



Analysis of forced convection heat transfer from a circular cylinder embedded in a porous medium

Gazy F. Al-Sumaily*, John Sheridan, Mark C. Thompson

Fluids Laboratory for Aeronautical and Industrial Research (FLAIR), Department of Mechanical and Aerospace Engineering, Monash University, Victoria 3800, Australia

ARTICLE INFO

Article history:

Received 22 February 2011
 Received in revised form
 29 August 2011
 Accepted 29 August 2011
 Available online 29 September 2011

Keywords:

Transient forced convection
 Porous media
 Non-Darcian effects
 Local thermal non-equilibrium

ABSTRACT

Time-dependent forced convection heat transfer from a single circular cylinder embedded in a horizontal packed bed of spherical particles under local thermal non-equilibrium condition is investigated numerically using the spectral-element method. The non-Darcian effects, i.e. inclusion of the effect of solid boundaries and inertia forces, and the effect of thermal dispersion, are taken into account. The influences of the presence of the porous material and its thermal properties: solid-to-fluid thermal conductivity ratio $k_r \in [0.01, 1000]$ and Biot number $Bi \in [0.01, 100]$, on the rates of heat transfer and the hydrodynamic and thermal responses, are examined for the Reynolds number range $Re_D \in [1, 250]$. These effects are quantified. Perhaps not surprisingly, the results show that the presence of the porous particles suppresses significantly the wakes behind the cylinder and enhances considerably the heat transfer. A comparison that is made between the one- and two-equation energy model predictions shows that the former model predicts a continuous increase in Nu_f against k_r ; however, the trend of Nu_f with k_r , for $k_r > 10$, is governed entirely by Bi when the latter model is used. Also, the increase in Bi decreases Nu_f and increases Nu_s , and high values of k_r or Bi lead to establishing a thermal equilibrium status in the porous bed.

© 2011 Elsevier Masson SAS. All rights reserved.

1. Introduction

There has been broad and considerable published research in the field of convection heat transfer in porous media. Excellent review articles and monographs have been provided by, for example, Ingham and Pop [5], Vafai [24], Pop and Ingham [17] and Nield and Bejan [15]. These indicate the level of understanding of momentum and heat transport in porous media. However, much of the preceding work on this topic has been directed to either convection near plane walls or in channels filled with porous media. To date there has been relatively limited published work on convective heat transfer from heated bodies of higher complexity, such as circular cylinders, embedded in porous media. Heat transfer from cylinders immersed in a fluid-saturated porous media has practical importance in many engineering applications such as compact heat exchangers, nuclear reactors and solar power collectors. In addition, most of the published studies on this specific subject has been devoted to either natural or mixed convection. Examples are the investigations carried out by Merkin [12], Cheng [2], Ingham and Pop [6], Badr and Pop [1], Pop and Cheng [16], Zhou and Lai [30], and Saeid [20]. Whereas, forced convection, although encountered frequently in applications, appears less studied.

The majority of studies conducted in the forced convection regime have used the simple Darcy model to relate the flow velocity to the applied pressure gradient. Sano [21] and Pop and Yan [18] used this model and presented analytical solutions for the energy equation in the boundary-layer region. In particular Sano presented an asymptotic solution of the unsteady energy equation for large and small values of Péclet number, while Pop and Yan obtained heat transfer rates for a cylinder and sphere as a function of the angular coordinate. Kimura [9] analytically and numerically examined transient forced convection from a cylinder placed in a porous layer with cross flow. The Nusselt number variation for the transient stage and at the steady state was obtained analytically. It was found that the length of the transient period to reach the convective steady state was inversely proportional to Péclet number. Layeghi and Nouri-Borujerdi [11] numerically analyzed the steady-state of the problem in the range of Péclet number ≤ 40 with constant Prandtl number equal to 1. In their analysis, the thermal field around the cylinder was found to be affected by the porosity of the porous medium and not by the permeability.

Other authors have used various types of extended Darcy models. Thevenin and Sadaoui [22] used the Darcy–Brinkman model to investigate forced convective flow over a cylinder immersed in a fibrous porous medium for a range of Reynolds number [1–100] to avoid the influence of thermal dispersion. It was revealed that the permeability of the porous medium does not have any effect on the

* Corresponding author. Tel.: +61 399051346.

E-mail addresses: gazy.alsumaily@monash.edu (G.F. Al-Sumaily), john.sheridan@monash.edu (J. Sheridan), mark.thompson@monash.edu (M.C. Thompson).

temperature field; however, the variation in the velocity field was found to be strongly dependent on it. Furthermore, heat transfer analysis for a single cylinder and an array of cylinders was performed by Layeghi and Nouri-Borujerdi [10] by using the Darcy and the Darcy–Brinkman models. The analysis was carried out with and without the presence of porous media at low Péclet number (≤ 40) for a single cylinder, and at intermediate Péclet number (≤ 300) for arrays of cylinders. It was concluded that the porous-medium models predict different results at low Darcy numbers. In addition, they found that more than 80% heat transfer enhancement can be obtained from the single cylinder by immersing it in a porous medium at high Darcy number. Moreover, by using the Darcy–Brinkman–Forchheimer (DBF) model, Murty et al. [13] investigated the effect of Reynolds, Darcy, and Forchheimer numbers on forced convective heat released from a circular cylinder embedded in a porous medium. They concluded that the effect of inertial forces on the Nusselt number depends on the permeability of the porous medium used.

A local thermal equilibrium (LTE) energy model, which is also called the one-equation energy model, was assumed in all the investigations mentioned, i.e., the temperature of the solid and the fluid phases are the same within the representative elementary volume. The porous medium is treated as a continuum by volume-averaging the properties of the two phases. However, various authors, for example by Vafai and Sozen [25] and Kaviany [8], have found the LTE assumption invalid for a number of applications involving convection in porous media. It is expected that when there is a significant difference between advection and conduction mechanisms in transferring heat, the deviation between the solid and fluid phase temperatures increases, and therefore the LTE model becomes progressively less valid. It was also noted by Pop and Cheng [16] that this approach may be questionable when the particle size in the solid porous matrix is comparable to or exceeds the thermal boundary layer thickness. Therefore, a local thermal non-equilibrium (LTNE) model, which is also called the two-equation energy model, should be incorporated. This model assigns individual local temperatures to the fluid and the solid, thus allowing heat transfer between the two phases.

It appears that the LTNE model has only been utilized by Rees et al. [19] and Wong et al. [28] to demonstrate how the thermal fields of the solid and fluid phases, and the rate of heat transfer around and from a horizontal circular cylinder, are affected by the absence of the LTE condition. Rees et al. examined the problem in the limit of high values of Péclet number. Their study was an analysis of forced convection in the boundary layer regime by reducing the governing equations to a parabolic partial differential system. Later, this study was supplemented by Wong et al. who investigated the same problem but at finite Péclet number by numerically solving the fully elliptic Darcy and two-equation energy models. In these studies the heat transfer in both phases was found to be increased by increasing the fluid-to-solid thermal conductivity ratio for all the values of the dimensionless interfacial heat transfer coefficient tested. This occurred with no effect of this coefficient on the trend of convective heat transfer from the heated cylinder with the conductivity ratio. However, it is expected to see an influence from the interfacial heat coefficient on this tendency, particularly for high values of solid thermal conductivity. Whereas, it was found that the interfacial coefficient increases the rate of heat transfer in the solid phase and decreases it in the fluid phase. Both of these investigations ignored non-Darcian effects and used the simple Darcy model, which is only valid for small Reynolds numbers ($O(1)$ or less) based on the pore scale. Also, they omitted the effect of thermal dispersion, which has a significant influence on the process of heat transfer in porous systems as explained in the literature.

In this paper, a more reliable flow model that incorporates non-Darcian effects, i.e., including the effects of solid boundaries, inertia and thermal dispersion, combined with the LTNE assumption, was

used to accurately predict the time-dependent forced convection heat transfer from a circular cylinder embedded in a horizontal packed bed of spherical particles. The objective of the present study is to investigate the influences of: porous media on the fluid flow and heat transfer enhancement; and the thermal properties, i.e. solid/fluid thermal conductivity ratio and the interfacial heat transfer coefficient, as represented by Biot number, of the porous medium on the heat transfer from the cylinder.

2. Mathematical formulation

The problem under consideration is unsteady forced convective flow over a circular cylinder immersed in a horizontal packed bed of spherical particles, as illustrated in Fig. 1. The fluid flow is assumed to be laminar and incompressible. The cylinder is isothermally heated at a constant temperature T_h and cooled by the incoming external flow at T_o . The confining horizontal walls have the same temperature T_w as the flow at the inlet. The blockage ratio of the bed is $D_{cy}/H = 0.25$, where D_{cy} is the cylinder diameter, which is considered the unit scale length, and H is the bed height. In analyzing the problem, the following assumptions are invoked: the porous medium is homogenous and isotropic, no heat generation occurs inside the porous medium, the inter-particle radiation heat transfer is ignored, the blockage ratio of the bed is small enough to neglect the channelling effect at the channel walls on the heat transfer from the cylinder surface, but local thermal equilibrium between the two phases is not assumed.

Based on these assumptions, the system of 2D governing equations of the average-volume continuity, Darcy–Brinkman–Forchheimer (DBF) momentum, and LTNE energy can be presented in the following vectorial form (Nield and Bejan [15], and Kaviany [8]):

$$\nabla \cdot \langle \mathbf{u} \rangle = 0, \quad (1)$$

$$\frac{\rho_f}{\varepsilon} \left[\frac{\partial \langle \mathbf{u} \rangle}{\partial t} + \frac{1}{\varepsilon} \langle (\mathbf{u} \cdot \nabla) \mathbf{u} \rangle \right] = -\frac{\mu_f \langle \mathbf{u} \rangle}{K} - \frac{\rho_f F \varepsilon}{\sqrt{K}} |\langle \mathbf{u} \rangle| \langle \mathbf{u} \rangle + \frac{\mu_f}{\varepsilon} \nabla^2 \langle \mathbf{u} \rangle - \nabla \langle \hat{p}_f \rangle, \quad (2)$$

$$\varepsilon (\rho c_p)_f \left[\frac{\partial \langle \hat{T}_f \rangle}{\partial t} + \langle \mathbf{u} \rangle \cdot \nabla \langle \hat{T}_f \rangle \right] = \nabla \cdot [k_{f,eff} \nabla \langle \hat{T}_f \rangle] + h_{sf} a_{sf} (\langle \hat{T}_s \rangle - \langle \hat{T}_f \rangle), \quad (3)$$

$$(1 - \varepsilon) (\rho c_p)_s \frac{\partial \langle \hat{T}_s \rangle}{\partial t} = \nabla \cdot [k_{s,eff} \nabla \langle \hat{T}_s \rangle] - h_{sf} a_{sf} (\langle \hat{T}_s \rangle - \langle \hat{T}_f \rangle), \quad (4)$$

while, the one-equation energy model can be written following:

$$(\rho c_p)_m \frac{\partial \langle \hat{T} \rangle}{\partial t} + \varepsilon (\rho c_p)_f [\langle \mathbf{u} \rangle \cdot \nabla \langle \hat{T} \rangle] = \nabla \cdot [k_{f,eff} \nabla \langle \hat{T} \rangle], \quad (5)$$

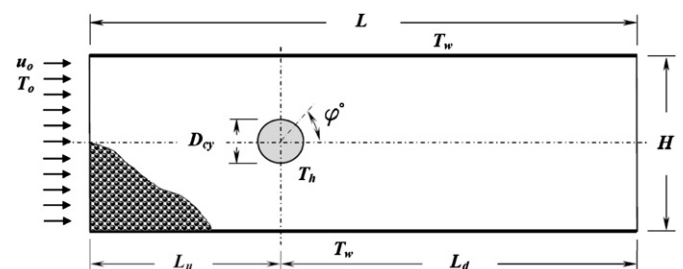


Fig. 1. Schematic diagram of the physical domain.

where, $|\langle \mathbf{u} \rangle| = \sqrt{\langle u^2 \rangle + \langle v^2 \rangle}$, and $(\rho c_p)_m = \varepsilon(\rho c_p)_f + (1-\varepsilon)(\rho c_p)_s$. The operator $\langle \dots \rangle$ denotes local volume average of a quantity. The Eqs. (1)–(5) are transformed into a non-dimensional form Eqs. (7)–(11) employing the following dimensionless variables,

$$x, y = \frac{\hat{x}, \hat{y}}{D_{cy}}, \quad \mathbf{u} = \frac{\hat{\mathbf{u}}}{u_o}, \quad t = \frac{\hat{t} u_o}{D_{cy}}, \quad \theta = \frac{\hat{T} - T_o}{(T_h - T_o)}, \quad P_f = \frac{\hat{P}_f}{\rho_f u_o^2} \quad (6)$$

$$\nabla \cdot \langle \mathbf{u} \rangle = 0, \quad (7)$$

$$\frac{\partial \langle \mathbf{u} \rangle}{\partial t} + \frac{1}{\varepsilon} \langle \langle \mathbf{u} \cdot \nabla \rangle \mathbf{u} \rangle = -\frac{\varepsilon}{Re_D Da} \langle \mathbf{u} \rangle - \frac{F \varepsilon^2}{\sqrt{Da}} |\langle \mathbf{u} \rangle| \langle \mathbf{u} \rangle + \frac{1}{Re_D} \nabla^2 \langle \mathbf{u} \rangle - \varepsilon \nabla \langle P_f \rangle, \quad (8)$$

$$\frac{\partial \langle \theta_f \rangle}{\partial t} + \langle \mathbf{u} \rangle \cdot \nabla \langle \theta_f \rangle = \frac{1}{\varepsilon Re_D Pr} \left[\frac{k_{f,eff,x}}{k_f} \frac{\partial^2 \langle \theta_f \rangle}{\partial x^2} + \frac{k_{f,eff,y}}{k_f} \frac{\partial^2 \langle \theta_f \rangle}{\partial y^2} \right] + \frac{Bi \cdot k_r}{\varepsilon Re_D Pr} (\langle \theta_s \rangle - \langle \theta_f \rangle), \quad (9)$$

$$\frac{\partial \langle \theta_s \rangle}{\partial t} = \frac{\alpha_r}{(1-\varepsilon) Re_D Pr} \nabla \cdot \left[\frac{k_{s,eff}}{k_s} \nabla \langle \theta_s \rangle \right] - \frac{Bi \cdot \alpha_r}{(1-\varepsilon) Re_D Pr} (\langle \theta_s \rangle - \langle \theta_f \rangle), \quad (10)$$

and, the dimensionless form of the one-equation energy model becomes:

$$\frac{\partial \langle \theta \rangle}{\partial t} + (1/C) [\langle \mathbf{u} \rangle \cdot \nabla \langle \theta \rangle] = \frac{1}{Re_D Pr \cdot C} \nabla \cdot \left[\frac{k_{f,eff}}{k_f} \nabla \langle \theta \rangle \right], \quad (11)$$

where, $C = \varepsilon + (1-\varepsilon)(k_r/\alpha_r)$, and k_r and α_r are the solid/fluid thermal conductivity and diffusivity ratios, k_s/k_f and α_s/α_f , respectively. In addition, the Reynolds, Darcy, Prandtl, and Biot numbers are defined, respectively, as:

$$Re_D = \frac{u_o D_{cy} \rho_f}{\mu_f}, \quad Da = \frac{K}{D_{cy}^2}, \quad Pr = \frac{\nu_f}{\alpha_f}, \quad Bi = \frac{D_{cy}^2 h_{sf} a_{sf}}{k_s}, \quad (12)$$

where, a_{sf} is the specific surface area of the packed bed. The permeability of the porous medium K and the geometric function F in the momentum equation are inherently tied to the structure of the porous medium. These are generally based on empirical fits from experimental findings, i.e., no universal representations exist. For a randomly packed bed of spheres such coefficients were reported by Ergun [4] and were expressed in terms of porosity ε and particle diameter d_p as follows:

$$K = \frac{\varepsilon^3 d_p^2}{150(1-\varepsilon)^2}, \quad F = \frac{1.75}{\sqrt{150\varepsilon^3}}. \quad (13)$$

The effective thermal conductivity of the fluid phase $k_{f,eff}$ is composed of a sum of the stagnant k_{st} and dispersion k_d

Table 2

Domain size study for the; (a) empty channel, and (b) porous channel at $k_r = 100$ and $Bi = 0.01$, for two values of $Re_D = 10$ and 250, with order of polynomial $p = 6$.

Domain	(a) Empty channel		(b) Porous channel			
	$Re_D = 10$		$Re_D = 10$		$Re_D = 250$	
	Nu_f	Nu_f	Nu_f	Nu_s	Nu_f	Nu_s
M1	5.057827	19.441979	7.984645	0.129630	69.705124	0.130727
M2	5.122665	19.539155	7.968639	0.128593	69.699884	0.129716
M3	5.153913	19.660151	7.965108	0.128553	69.698501	0.129681
M4	5.153913	19.660764	7.965108	0.128553	69.698501	0.129681

conductivities: $k_{f,eff(x,y)} = k_{st} + k_d(x,y)$. In this study the stagnant conductivity depends on the conductivities of the fluid and the solid phases, and is obtained from the semi-theoretical model of Zehner and Schluender [29]:

$$\frac{k_{st}}{k_f} = (1 - \sqrt{1-\varepsilon}) + \frac{2\sqrt{1-\varepsilon}}{1-\lambda B} \times \left[\frac{(1-\lambda)B}{(1-\lambda B)^2} \ln(\lambda B) - \frac{B+1}{2} - \frac{B-1}{1-\lambda B} \right]. \quad (14)$$

where $\lambda = 1/k_r$ and $B = 1.25[(1-\varepsilon)/\varepsilon]^{10/9}$. Whereas, the dispersion conductivity that incorporates the additional thermal transport due to the fluid's tortuous path around the solid particles is determined in both longitudinal and lateral directions based on the experimental correlation reported by Wakao and Kaguei [26], and is given by:

$$\frac{k_{dx}}{k_f} = 0.5Pr \left(\frac{\rho_f u_o d_p}{\mu_f} \right), \quad \frac{k_{dy}}{k_f} = 0.1Pr \left(\frac{\rho_f u_o d_p}{\mu_f} \right). \quad (15)$$

The effective thermal conductivity for the solid phase consists merely of the phase fraction component which is the stagnant component since the solid phase is stationary:

$$k_{s,eff} = (1-\varepsilon)k_s. \quad (16)$$

The DBF momentum Eq. (8) can be transformed to the Navier-Stokes equation by taking $\varepsilon = 1$ and $K = \infty$, and the one-equation energy model 11 to the standard fluid energy equation by taking $C = 1$ and $k_{f,eff} = k_f$, to predict the fluid flow and thermal fields, respectively, in the channel in the absence of the porous medium. Dirichlet boundary conditions, for the pertinent variables, i.e., the velocity and temperature, are imposed on the inlet and solid boundaries, while Neumann boundary conditions are imposed at the outlet. Thus, the non-dimensional initial and boundary conditions can be expressed mathematically as:

$$\begin{aligned} \text{at } t=0: & u = v = \theta_f = \theta_s = 0 \\ \text{at } t>0: & u = u_o, v = \theta_f = \theta_s = 0 \quad \text{at } (x=0, 0 < y < H) \\ & \frac{\partial u}{\partial x} = \frac{\partial \theta_f}{\partial x} = \frac{\partial \theta_s}{\partial x} = v = 0 \quad \text{at } (x=L, 0 < y < H) \\ & u = v = 0 = \theta_f = \theta_s = 0 \quad \text{at } (0 < x < L, y=0 \text{ and } H) \\ & u = v = 0, \theta_f = \theta_s = 1 \quad \text{at cylinder boundary} \end{aligned} \quad (17)$$

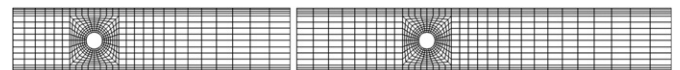


Fig. 2. Typical macro-mesh for; (left) M2 domain and (right) M3 domain.

Table 1

Four physical domains with their upstream and downstream lengths.

Domain	L_u	L_d	Macro-elements	Macro-nodes
M1	$3D_{cy}$	$10D_{cy}$	560	615
M2	$5D_{cy}$	$12D_{cy}$	624	683
M3	$8D_{cy}$	$15D_{cy}$	720	785
M4	$8D_{cy}$	$20D_{cy}$	800	870

Table 3
Grid resolution study of the computational domain M2 for different values of k_r and Bi by varying p within the range 2–8, at $Re_D = 1.0$.

p	$k_r = 0.01$		$k_r = 1000$		$Bi = 0.01$		$Bi = 100$	
	Nu_f	Nu_s	Nu_f	Nu_s	Nu_f	Nu_s	Nu_f	Nu_s
2	2.09393	0.20872	1.94596	0.12474	2.54463	0.12691	2.45330	0.23578
3	2.08482	0.20838	1.94019	0.12437	2.53591	0.12655	2.44535	0.23510
4	2.08265	0.20809	1.93520	0.12405	2.53301	0.12623	2.44249	0.23479
5	2.08122	0.20789	1.93199	0.12385	2.53100	0.12603	2.44049	0.23459
6	2.08012	0.20774	1.92979	0.12371	2.52949	0.12589	2.43899	0.23445
7	2.07933	0.20764	1.92818	0.12360	2.52840	0.12578	2.43790	0.23434
8	2.07871	0.20756	1.92696	0.12352	2.52756	0.12570	2.43706	0.23426

Heat transfer characteristics are evaluated based on the time-mean local and average Nusselt numbers along the heated cylinder for the fluid and solid phase as follows:

$$Nu_{f\phi} = \frac{h_{cy} D_{cy}}{k_f} = \frac{-k_{f,eff} \left[\partial \hat{T}_f / \partial n \right] D_{cy}}{k_f (T_h - T_o)}, \quad Nu_f = \frac{1}{S} \int_0^S Nu_{f\phi} ds,$$

$$Nu_{s\phi} = \frac{h_{cy} D_{cy}}{k_s} = \frac{-k_{s,eff} \left[\partial \hat{T}_s / \partial n \right] D_{cy}}{k_s (T_h - T_o)}, \quad Nu_s = \frac{1}{S} \int_0^S Nu_{s\phi} ds, \quad (18)$$

where n and s denote to the normal and tangential directions at the cylinder surface, respectively, and S is the circumference of the cylinder. Consequently, the time-mean average total Nusselt number Nu_t is defined as the summation of Nu_f and Nu_s :

$$Nu_t = Nu_f + Nu_s. \quad (19)$$

Pressure drop is calculated as:

$$\Delta P_f = |\rho_f u_o^2 (P_{f,out} - P_{f,o})|, \quad (20)$$

where the subscripts *out* and *o* refer to the outlet and inlet of the channel.

3. Numerical method of solution

Eqs. (7)–(11) have been solved using a spectral-element method, which is essentially a high-order finite-element method, see Karniadakis et al. [7] and Thompson et al. [23]. In terms of the spatial discretisation, this method employs tensor-product Lagrange polynomials, associated with Gauss–Legendre–Lobatto quadrature

points, as shape functions over each quadrilateral element. In this way, the spatial resolution can be varied by either changing the number of quadrilateral elements (h -refinement), or by changing the order of the Lagrange polynomial shape functions (p -refinement). For the current study, a polynomial order of $p = 6$ was employed.

For the temporal discretisation, a two- and three-step time-splitting scheme, described in Chorin [3], Karniadakis et al. [7] and Thompson et al. [23], is used for the energy and momentum equations. For the energy equations, this results in separate equations being formed for the non-linear advection term and the linear diffusion term. For the momentum equations, a third equation is required for the pressure. A Poisson equation is formed for the pressure term by enforcing continuity at the end of the pressure sub-step. The non-linear advection equation is solved using a third-order Adams–Bashforth method, and the linear diffusion equation is solved using a second-order Crank–Nicholson method. Because of the non-linear coupling between the equations, it is necessary to iterate over each time-step. Iteration is required until convergence is achieved. In the present study, it is assumed that this occurs when $\langle \mathbf{u} \rangle$ velocity components and Nu_f and Nu_s in two consecutive iterations differ by less than the convergence criterion of 10^{-10} .

3.1. Domain and grid independency of the results

Tests were conducted to ensure that the numerical results obtained are independent of the domain size and the spatial grid resolution. Domain size and grid resolution studies were undertaken for the configuration of the circular cylinder mounted between two parallel walls as shown in Fig. 1. Nu_f and Nu_s were monitored in these studies as an indicator of convergence. The study of domain size was performed for four physical domains M1, M2, M3, and M4, according to their upstream L_u and downstream L_d

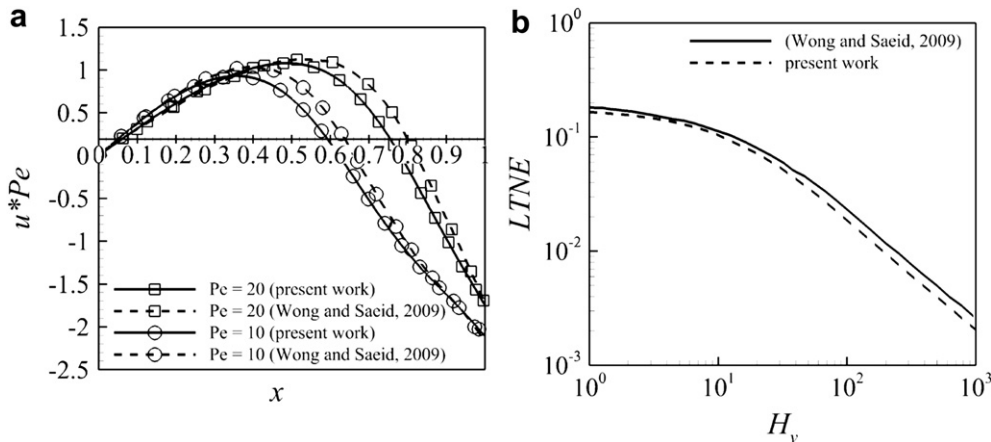


Fig. 3. Comparison between two numerical models: the present model and the model used by Wong and Saeid (2009); (a) for the variation of (u -velocity \times Pe) at $y = 0.002$ along the heat source, for two values of $Pe = 10$ and 20 , with interfacial convective heat transfer coefficient and porosity-scaled fluid/solid thermal conductivity ratio $H_v = 1.0$ and $K_r = 1.0$, respectively, and (b) for the variation of $LTNE$ against H_v at $Pe = 100$ and $K_r = 1.0$.

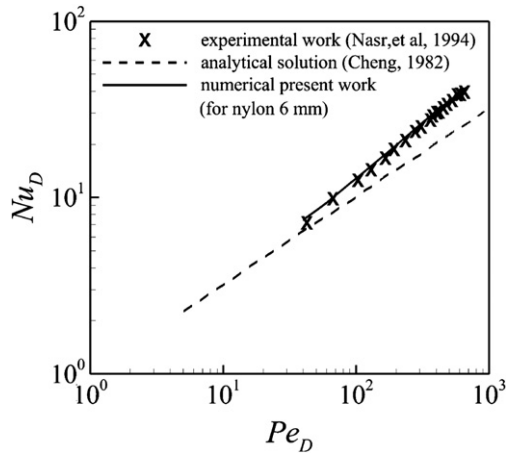


Fig. 4. Comparison between the present algorithm with the experimental work done by Nasr et al. (1994), for the air forced convection heat transfer around a circular cylinder, $D = 12.7$ mm, embedded in a packed bed of nylon spherical particles, $d_p = 6.35$ mm, with porosity $\varepsilon = 0.37$ and solid/fluid thermal conductivity ratio $k_r = 8.7$.

lengths from the centre of the cylinder as shown in Table 1. To sufficiently resolve the higher temperature gradients near the heated cylinder the macro-element distribution was concentrated around its surface. The macro-mesh resolution is decreased in both the upstream and downstream directions to the inlet and outlet boundaries where gradients are smaller. To capture the boundary layers in the y -direction a finer mesh is employed near the walls with coarsening towards the core of the channel. The four domains were examined at two values of $Re_D = 10$ and 250, with polynomial order $p = 6$. The results of the study presented in Table 2, showed that the M2 and M3 domains, described in Fig. 2, are appropriate choices for the porous and empty channels, respectively, with numerical errors less than 0.1% as measured by Nusselt number convergence.

A grid resolution study was undertaken for the M2 domain at $Re_D = 1$ and 250 for the following parameters: $k_r = 0.01$ and 1000; $Bi = 0.01$ and 100. This was done by varying p within the range 2–8, while keeping the macro-element layout the same, in order to ascertain at what spectral resolution the solution becomes grid independent and subsequently which resolution provides a satisfactory compromise between accuracy and computational expense. An advantage of the spectral-element method is the ability to set polynomial order p at run-time, allowing resolution studies to be

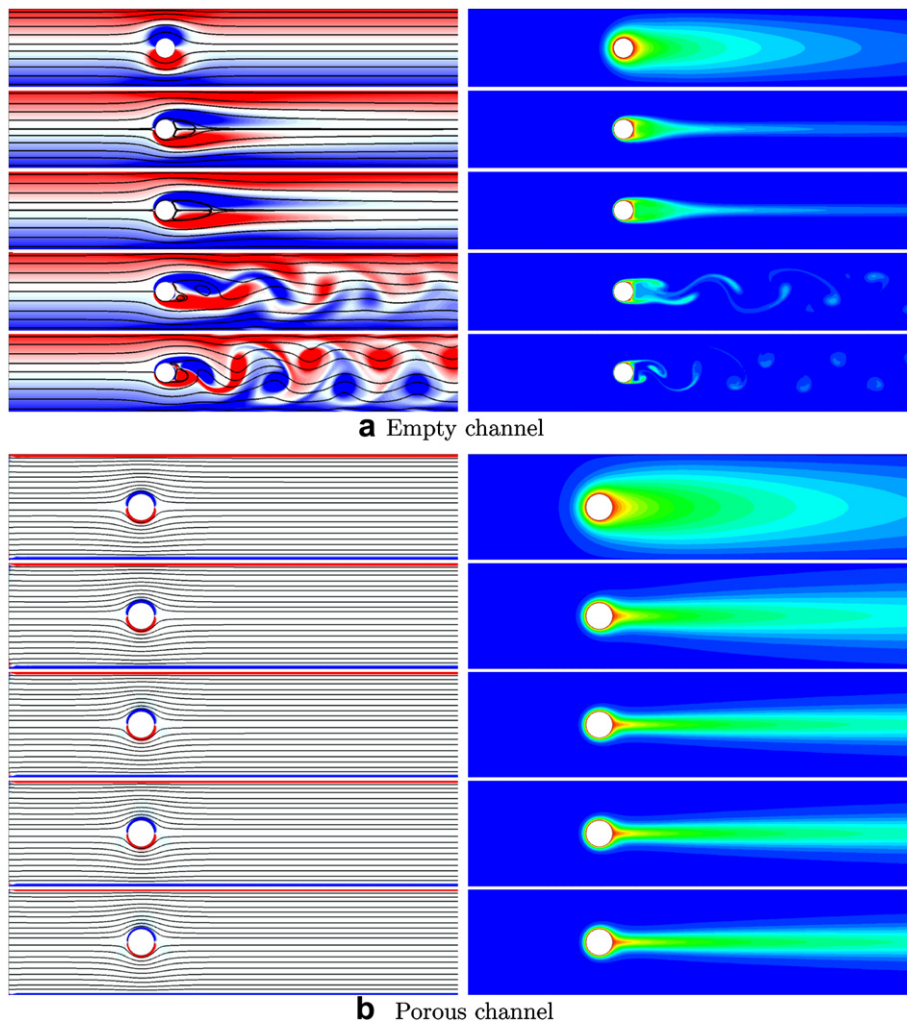


Fig. 5. Vorticity with streamlines (left), and isotherms (right), around a heated circular cylinder mounted in a horizontal; (a) empty channel, (b) packed bed of spheres using the two-equation thermal model, at $k_r = 1.0$ and $Bi = 1.0$, for different Re_D , from top to bottom, 1.0, 40, 70, 100, and 250, with $Pr = 7.0$. Red (blue) contours represent positive (negative) vorticity and hot (cold) temperatures. (For interpretation of the references to colour in this figure legend, the reader is referred to the web version of this article.)

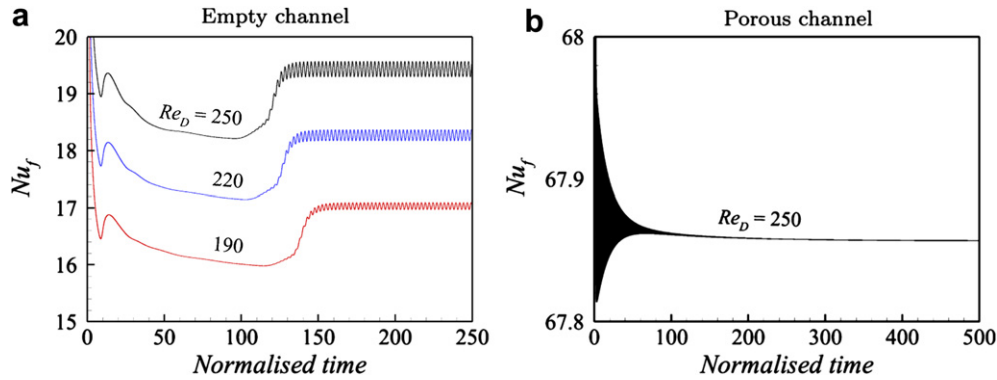


Fig. 6. Plots of the transient average fluid Nusselt number Nu_f from a heated cylinder placed in (a) an empty channel at $Re_D = 190, 220,$ and $250,$ and (b) a porous channel using the two-equation thermal model at $k_r = 1.0, Bi = 1.0,$ and $Re_D = 250.$

performed more easily. The results showed that Nu_f and Nu_s are converged by $p = 6$ with a relative error of less than 0.5%. Examples of these results for the case of $Re_D = 1$ are shown in Table 3.

The numerical simulations were performed at a timestep $\Delta t = 0.001$ (determined by a Courant time-step restriction), on the Monash (University) Sun Grid (MSG) and National Computational Infrastructure (NCI) high-performance computers.

3.2. Verification of the numerical method

In order to validate the implementation, results from this code were compared to previously published numerical and experimental results. First, velocity and temperature data for a cooling air jet impinging on an isothermal heated surface immersed in a confined porous channel under the LTNE condition was calculated and compared to the data for the identical problem presented in Wong and Saeid [27]. For this data, the Rayleigh number is $Ra = 100,$ the Darcy number is $Da = 10^{-3},$ and the porosity is $\varepsilon = 0.87.$ Fig. 3a presents the velocity distribution close to the wall being impinged upon, and Fig. 3b presents the LTNE parameter, defined as:

$$LTNE = \frac{\sum_N |\theta_s - \theta_f|}{N}, \quad (21)$$

where N is the total number of nodes in the domain. This is a simple measure of the mean difference between the fluid and solid over the domain. The agreement of both the velocity and temperature data is very good, although there are some differences, which are yet

unexplained. Second, the numerical results were benchmarked against experimental results obtained by Nasr et al. [14] for the air forced convection heat transfer around a circular cylinder embedded in a packed bed of nylon spherical particles. The comparison is presented in Fig. 4. As recommended in their paper, the model of Zehner and Schluender [29] was used to calculate the effective stagnant thermal conductivity in the energy equation while the dispersion-enhanced conductivity was neglected. The porous medium was treated as a continuum by volume-averaging the thermal diffusivity of the solid and fluid phases. There is clearly good agreement between the numerical predictions, the experimental results and, as a further comparison, with the analytical solutions made by Cheng [2] for mixed convection about a horizontal cylinder embedded in a fluid-saturated porous medium. Cheng obtained similarity solutions using the Darcy model in the boundary-layer region.

4. Results and discussion

The effect of the presence of porous media on fluid flow and forced convection heat transfer around a circular cylinder mounted in a horizontal channel is investigated for the Reynolds number range $Re_D \in [1, 250].$ The effects of the porous medium's thermal properties: solid-to-fluid thermal conductivity ratio $k_r \in [0.01, 1000]$ and Biot number $Bi \in [0.01, 100],$ on the convective and conductive heat transfer from the heated cylinder to the fluid and solid phases, respectively, and the thermal response inside the porous channel, are also examined using the two-equation energy model. Following

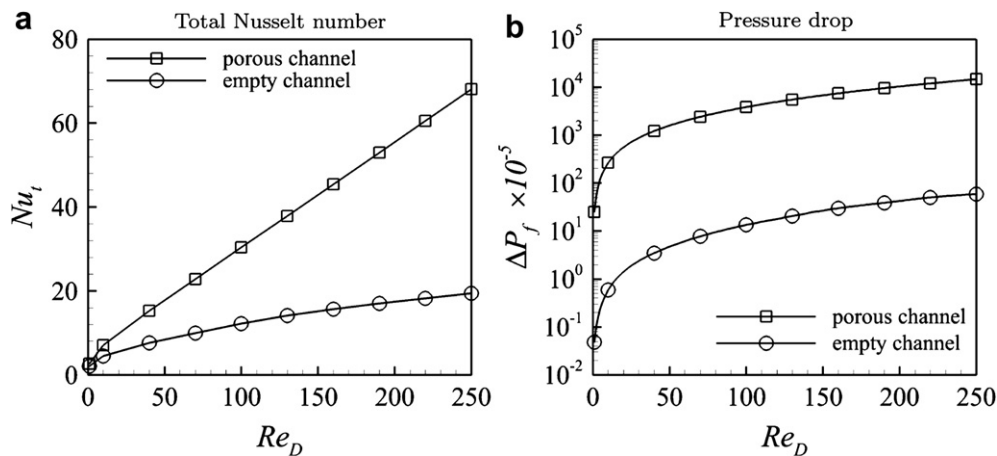


Fig. 7. The variation of (a) the total time-mean average Nusselt number Nu_t from a heated cylinder embedded in, and (b) the pressure drop ΔP_f through, a packed bed of spheres using the two-equation thermal model at $k_r = 1.0$ and $Bi = 1.0$ (\square), and an empty channel (\circ), against $Re_D.$

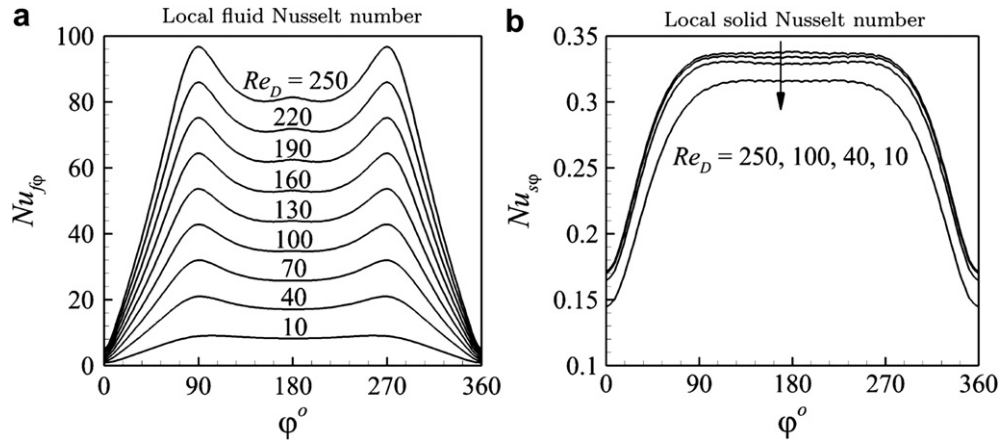


Fig. 8. The distribution of the time-mean local fluid and solid Nusselt number, $Nu_{f,\phi}$ and $Nu_{s,\phi}$, respectively, over the periphery of a heated cylinder embedded in a packed bed of spheres, calculated by using the two-equation energy model at $k_r = 1.0$ and $Bi = 1.0$, and for different Re_D .

that a comparison between the results obtained by the one- and two-equation energy models is made. The numerical simulations have been performed at fixed values of $Pr = 7$, $\alpha_r = 1.0$, $D_{cy}/d_p = 20$, $\varepsilon = 0.5$, and $Da = 8.333 \times 10^{-6}$ for all cases.

4.1. Effect of the presence of porous media

When a bluff body is placed in an uniform stream of fluid for a sufficiently high Re_D , two separated shear layers are formed, one on each side of the body, the vorticity of the two layers being opposite. This is shown in Fig. 5a for a circular cylinder placed in an uniform stream of water flowing inside a horizontal channel for $1.0 > Re_D > 250$. Fig. 5b shows the influence of packing the channel with porous particles on the vorticity of the separated shear layers formed around and behind the cylinder, and the thermal response. In Fig. 5, the fields of fluid flow and temperature are described in terms of vorticity with streamlines and isotherms, respectively, inside the empty and packed channels. In the empty channel, a steady wake behind the cylinder is observed for Re_D up to 100, with a clear increase in the length of the wake with increasing Re_D . For $Re_D \geq 100$, vortex shedding occurs and causes hydrodynamic and thermal periodic wakes downstream of the cylinder. However, the figure demonstrates how the porous medium suppresses shedding due to the high frictional and inertial resistances offered by the matrix of the porous particles. Within the chosen Re_D range, it is shown that the effect of Re_D on the thicknesses of the

hydrodynamic boundary layers is almost negligible in the porous channel, but it has a considerable influence on the thermal boundary layers. Fig. 6 displays the time evolution of the average fluid Nusselt number Nu_f from the cylinder in both channels at selected values of Re_D . Unsteady time-periodic behaviour of Nu_f in the empty channel can be seen, with an increase in both the amplitude and frequency of the vortex shedding as Re_D is increased. However, after the transient has decayed a steady Nu_f is obtained in the porous channel even at the highest value of $Re_D = 250$.

The total heat transfer rate Nu_t from the cylinder and the pressure drop ΔP_f over the length of the channel with and without the presence of the porous medium, are presented in Fig. 7. It indicates that the particles serve as effective enhancers for forced convection heat transfer, particularly at high Re_D (up to four times at $Re_D = 250$ compared with the empty channel). This is due to the influence of thermal dispersion, where high Re_D generates strong convection effects and high thermal mixing in the fluid phase, which results in higher Nu_f . However, the enhanced heat transfer obtained from the porous material is at the expense of a significantly increased unfavourable pressure drop in the packed bed. Thus, the figure illustrates that the porous medium increases ΔP_f several thousand fold compared with the empty channel. In addition, the positive influence of Re_D on Nu_t in the porous channel is more significant than that in the empty channel. However, interestingly the positive influence of Re_D on the ΔP_f in the porous channel is found to be significantly less than that in the empty channel. Hence, in the

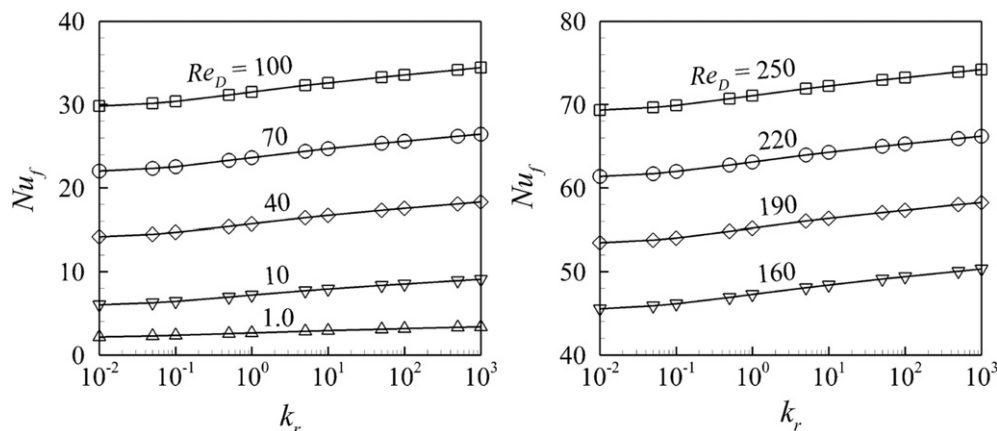


Fig. 9. Effect of the solid/fluid thermal conductivity ratio k_r of the porous channel on the time-mean average fluid Nusselt number Nu_f from a heated cylinder, and estimated by using the one-equation energy model, at selected values of Re_D .

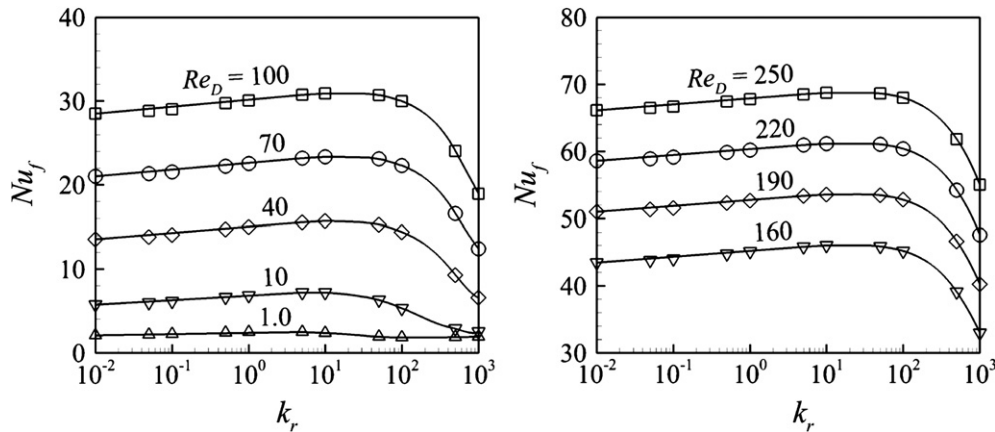


Fig. 10. Effect of the solid/fluid thermal conductivity ratio k_r of the porous channel on the time-mean average fluid Nusselt number Nu_f from a heated cylinder, and estimated by using the two-equation energy model, at $Bi = 1.0$ and selected values of Re_D .

porous channel, Nu_t increases roughly by 20 times and the pressure drops approximately by 600 times, by increasing Re_D from 1 to 250; while, in the empty channel, there is almost 4 times augmentation in Nu_t with 1250 times drop in pressure, for the same increase in Re_D .

Fig. 8 displays the distributions of the time-mean local fluid and solid Nusselt number, $Nu_{f\phi}$ and $Nu_{s\phi}$, respectively, on the heated surface of the cylinder embedded in the porous bed, from the rear stagnation point $\phi^\circ = 0^\circ$ anticlockwise from the flow direction, calculated by using the two-equation energy model at $k_r = 1.0$ and $Bi = 1.0$, and at different Re_D . These distributions show symmetric profiles about the streamwise axis of the cylinder. They reveal that the maxima $Nu_{f\phi}$ which are generally expected to occur in the regions of the highest velocity gradients that cause highest temperature gradients or around the front stagnation point where the fluid is impinging, are observed to be at the top and bottom of the cylinder, i.e., $\phi^\circ = 90^\circ$ and $\phi^\circ = 270^\circ$. The values of these two peaks are shown to increase with increasing Re_D . Whereas, the minimum $Nu_{f\phi}$ occurs at the rear stagnation point due to the expansion of the fluid thermal boundary layer behind the cylinder. However, the figure shows a different circumferential variation for $Nu_{s\phi}$, hence, it is almost flat on the most locations of the cylinder's periphery, $\phi^\circ = 90^\circ - 270^\circ$, and strongly independent on Re_D . Also, the values of $Nu_{s\phi}$ are much lower, approximately 200–300 times at $Re_D = 250$, than those of $Nu_{f\phi}$.

4.2. Effect of the thermal properties of porous media

It is well publicised in the literature that heat transfer can be increased by using porous media with higher thermal conductivity. However, the question can be raised: is this always the case? Figs. 9 and 10 which exhibit the effect of k_r on the time-mean average fluid Nusselt number Nu_f using the one- and two-equation energy models, respectively, at different Re_D , may answer this question. By ignoring the convective heat transfer between the two phases, and considering the porous bed as a quasi-continuum, the one-equation model predicts that the higher the k_r , the higher the Nu_f , as shown in Fig. 9. This is due to the high solid thermal conductivity results in high contact conduction. However, interestingly, Fig. 10 exposes a different trend of Nu_f with k_r when the two-equation model is used. It shows that Nu_f increases with increasing k_r , but only up to an intermediate value 10; following this, there is a considerable decrease in Nu_f . The decrease in Nu_f for $k_r > 10$ is because the large contribution of heat transfer from the solid phase to the fluid phase by convection at $Bi = 1.0$ which is taken into account in this model. This contribution produces a highly uniform fluid thermal field

around the hot cylinder, which causes a decrease in temperature gradient and then a reduction in Nu_f . Where, Fig. 11 reveals that the time-mean average solid Nusselt number Nu_s is not considerably influenced by k_r until this contribution starts to be effective at the above-mentioned intermediate value of k_r . Thus, it can be seen that after this value, Nu_s begins decreasing towards a minimum value at the highest value of k_r . This is because a high k_r means a low conductive thermal resistance within the solid phase, and consequently a high transient conductive heat transfer which seems to be larger than its contribution to the fluid phase to produce a highly uniform solid thermal field around the cylinder.

Table 4 shows the variations of Nu_f and Nu_s with Bi when $k_r = 10$, for different values of Re_D . It reveals that the low rates of Nu_f are produced when Bi is large. This is as expected since it means there is high heat transfer between the two phases (from the solid to the fluid at $k_r = 10$). This also could explain the better heat conduction Nu_s within the solid phase when Bi is increased. However, small values of Bi correspond to poor transfer of heat to/from the solid phase, which enables its thermal field to be effectively independent of the fluid thermal field.

Isotherms of the steady-state fluid and solid thermal fields with varying k_r and Bi are shown in Fig. 12, when $Re_D = 10$. Clearly, the isotherms for the two phases are significantly altered when k_r increases, where their thermal boundary layers enlarge in the transverse direction and shorten in streamwise direction. This causes

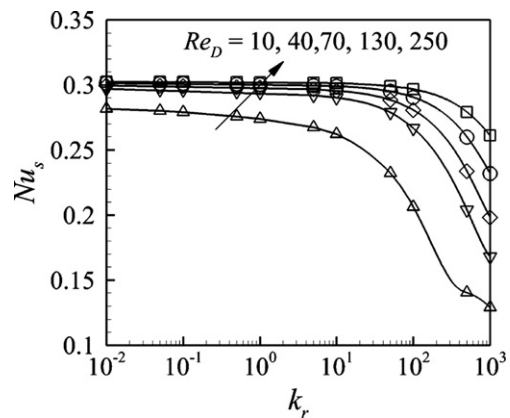


Fig. 11. Effect of the solid/fluid thermal conductivity ratio k_r of the porous channel on the time-mean average solid Nusselt number Nu_s from a heated cylinder, and estimated by using the two-equation energy model, at $Bi = 1.0$ and selected values of Re_D .

Table 4Values of Nu_f and Nu_s as a function of Bi at different Re_D when $k_r = 10$.

Bi	$Re_D = 1.0$		$Re_D = 10$		$Re_D = 40$		$Re_D = 100$		$Re_D = 250$	
	Nu_f	Nu_s	Nu_f	Nu_s	Nu_f	Nu_s	Nu_f	Nu_s	Nu_f	Nu_s
0.01	2.771	0.1256	7.544	0.1287	15.948	0.1294	31.123	0.1296	68.899	0.1297
0.05	2.686	0.1317	7.499	0.1454	15.922	0.1484	31.102	0.1491	68.881	0.1494
0.1	2.620	0.1372	7.458	0.1614	15.898	0.1668	31.082	0.1681	68.864	0.1686
0.5	2.433	0.1553	7.289	0.2259	15.785	0.2437	30.990	0.2483	68.781	0.2503
1.0	2.360	0.1628	7.175	0.2621	15.700	0.2901	30.918	0.2977	68.716	0.3010
5.0	2.252	0.1740	6.845	0.3446	15.401	0.4116	30.650	0.4323	68.466	0.4423
10	2.230	0.1763	6.713	0.3718	15.249	0.4601	30.503	0.4893	68.323	0.5040
50	2.208	0.1786	6.525	0.4068	14.966	0.5361	30.198	0.5861	68.009	0.6140
100	2.205	0.1789	6.490	0.4126	14.895	0.5521	30.112	0.6087	67.912	0.6414

an elliptical thermal plume to be generated around the circular cylinder at $k_r = 1000$. However, the figure shows that the fluid temperature distribution is not affected significantly by changing Bi , but there is a clear influence from Bi on the temperature distribution of the solid phase, which seems to be totally isolated from the fluid phase at $Bi = 0.01$. Interestingly, the figure illustrates that at very high k_r or Bi , the fluid and solid phases have effectively identical temperature fields, which indicates the establishment of a thermal equilibrium state in the porous system.

To demonstrate the role that Bi plays to change the influence of k_r on Nu_f , the variation of Nu_f versus k_r at various values of Bi is presented in Fig. 13 at $Re_D = 40$ and 250. Two main findings can be seen in this figure: first, the trend of Nu_f against k_r is independent of Bi when $k_r \leq 1.0$; however, it becomes dependent highly on Bi when $k_r > 1.0$. For example, for $k_r \leq 1.0$, there is only one increased trend of Nu_f with k_r for the entire range of Bi , while for $k_r > 1.0$, Nu_f can be increased or decreased depending on the value of Bi . This finding was confirmed by Rees et al. [19]. Second, the value of Nu_f is not

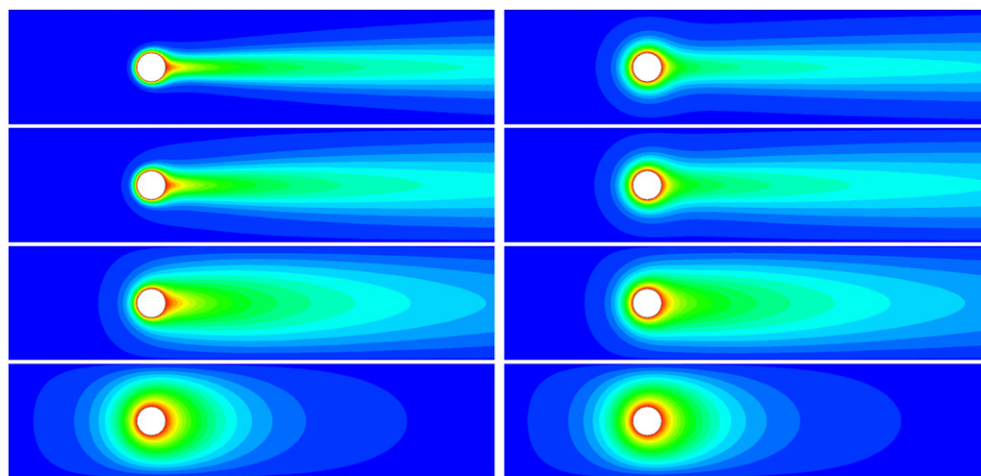
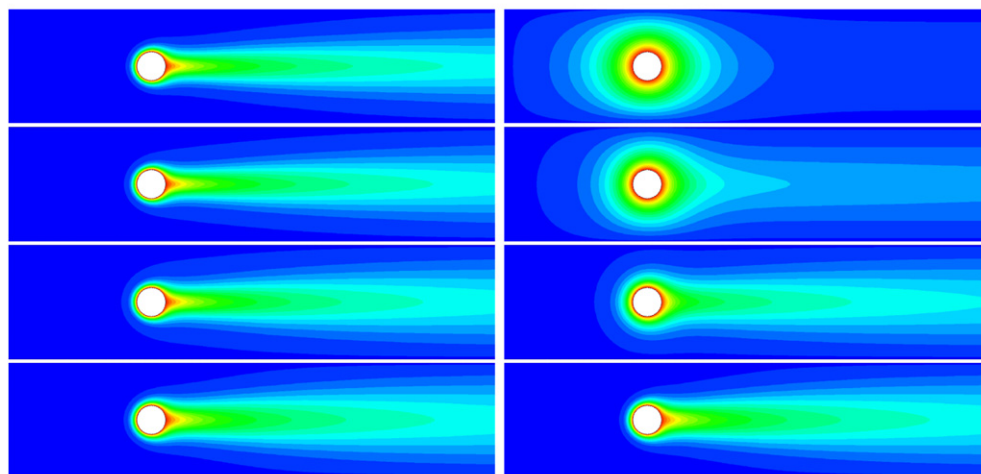
**a** for different k_r at $Bi = 1.0$ **b** for different Bi at $k_r = 10$

Fig. 12. Fluid (left) and solid (right) isotherms, around a heated circular cylinder immersed in a horizontal packed bed of spheres for different; (a) k_r , from top to bottom 0.01, 10, 100, and 1000, at $Bi = 1.0$, (b) Bi , from top to bottom 0.01, 0.1, 1.0, and 100, at $k_r = 10$, using the two-equation thermal model, at $Re_D = 10$ and $Pr = 7.0$. Red (blue) contours represent hot (cold) temperatures. (For interpretation of the references to colour in this figure legend, the reader is referred to the web version of this article.)

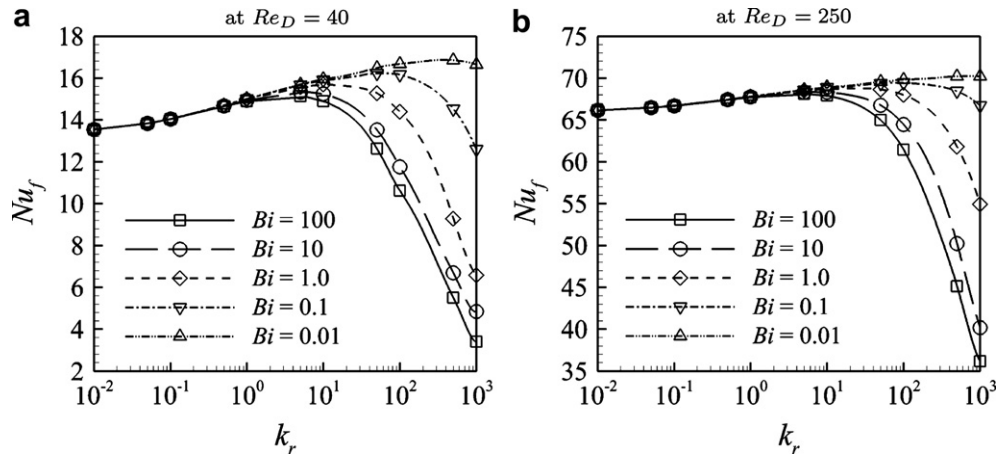


Fig. 13. The variation of the time-mean average fluid Nusselt number Nu_f versus the solid/fluid thermal conductivity ratio k_r at different values of Bi , and for two selected values of Re_D , (a) 40 and (b) 250.

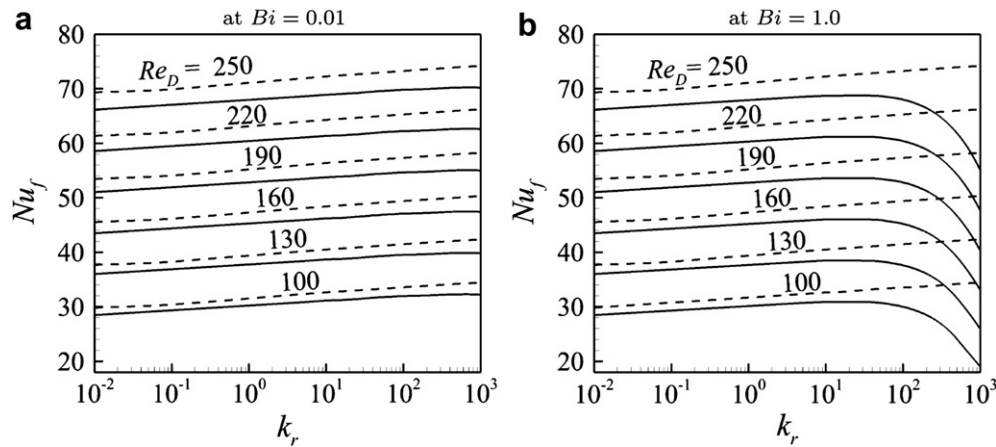


Fig. 14. Comparison between the one-equation (dash line) and the two-equation (solid line) energy models for the variation of Nu_f against k_r , for $Re_D = 100$ –250 in steps of 30, and at two values of Bi , (a) 0.01 and (b) 1.0.

influenced entirely by Bi for $k_r \leq 1.0$; however, it decreases as Bi increases for $k_r > 1.0$ as shown prior in Table 4 at $k_r = 10$. The reason for both of these points is the low rates of the transient conductive heat transfer in the solid phase caused by the high conductive thermal resistance at low solid thermal conductivity.

A comparison between the one- and two-equation energy models for the variation of Nu_f for different key parameters, namely: Re_D , k_r , and Bi , is described in Fig. 14. It is clear that the one-equation model always generate Nu_f higher than those predicted by the two-equation model. It may be due to the continuum assumption in the one-equation model to calculate the thermal properties of the porous medium. Also, the figure illustrates that the discrepancy between the results of Nu_f of the two models increases with increasing Re_D , increasing k_r at high Bi , or increasing Bi for $k_r > 1.0$.

5. Conclusion

The results presented here provide a better understanding of the influences of the presence of a porous medium of spherical particles, and its thermal properties, i.e., solid/fluid thermal conductivity ratio and Biot number, on the rates of heat transfer and the hydrodynamic and thermal behaviour around a heated circular cylinder mounted in a horizontal channel. Perhaps not surprisingly, the results show that the presence of the porous particles alters

significantly the unsteady hydrodynamic and thermal behaviour inside the channel, where it suppresses the wakes formed behind the cylinder and produces an unidirectional steady flow. Although a considerable heat transfer enhancement can be achieved by packing the channel with porous material, this is at the expense of a several thousand fold increase in pressure drop.

It is found that a continuous increase in Nu_f against k_r is predicted by using the one-equation energy model; however, by using the two-equation energy model, the trend of Nu_f with k_r , for $k_r > 10$, is entirely governed by Bi . Also, the increase in Bi decreases Nu_f and increases Nu_s , and high values of k_r or Bi lead to establishing a thermal equilibrium status in the porous bed. The study also shows that the effect of Re_D on Nu_f is much more significant than that of k_r and Bi due to the effect of thermal dispersion; therefore, for all cases the values of Nu_f are seen to be always much higher, by at least two order of magnitudes at $Re_D = 250$, than those of Nu_s . The comparison that is made between the two energy models for the results of Nu_f concludes that the one-equation model predicts Nu_f higher than that estimated by the two-equation model, and the difference between them increases as Re_D increases, k_r increases at high Bi , or Bi increases but only for $k_r > 1.0$.

In spite of the fact that the present study is related to packed bed of spheres, its results can be generalized and used for other types of porous media.

Acknowledgement

This research was supported in part by the Monash e-Research Centre and ITS-Research Support Services through the use of the Monash Sun Grid cluster, and Philip Chan, Senior e-Research Software Specialist ITS-Research Support Services, Monash e-Research Centre. The research was also supported by CPU time grant N67 on the National Computational Infrastructure (NCI) facilities.

Nomenclature

a_{sf}	specific interfacial area (m^{-1}).
Bi	Biot number, $Bi = h_{sf} a_{sf} D_{cy}^2 / k_s$.
c_p	specific heat capacity, (J/kg K).
d_p	particle diameter, (m).
D_{cy}	cylinder diameter, (m).
Da	Darcy number, $Da = K / D_{cy}^2$.
F	geometric function, $F = 1.75 / \sqrt{150 \varepsilon^3}$.
h_{cy}	cylinder surface heat transfer coefficient, ($\text{W/m}^2 \text{K}$).
h_{sf}	interfacial heat transfer coefficient, ($\text{W/m}^2 \text{K}$).
H	channel height, (m).
k	thermal conductivity, (W/m K).
k_r	solid/fluid thermal conductivity ratio, $k_r = k_s / k_f$.
K	permeability of the porous medium, $K = \varepsilon^3 d_p^2 / 150 (1 - \varepsilon)^2$, (m^2).
L	channel length, (m).
Nu	time-mean average Nusselt number.
Nu_φ	time-mean local Nusselt number.
p	Lagrangian polynomial order.
\hat{P}_f	fluid pressure, (N/m^2).
P_f	dimensionless fluid pressure.
Pr	Prandtl number, $Pr = \nu_f / \alpha_f$.
Re_D	Reynolds number, $Re_D = u_o \rho_f D_{cy} / \mu_f$.
t	time, (sec).
\hat{t}	dimensionless time.
\hat{T}	temperature, (K).
$\hat{\mathbf{u}}$	vectorial fluid velocity, (m/s).
\mathbf{u}	dimensionless vectorial fluid velocity, $\mathbf{u} = \hat{\mathbf{u}} / u_o$.
\hat{u}	horizontal velocity component, (m/s).
u	dimensionless horizontal velocity component.
u_o	inlet horizontal fluid velocity, (m/s).
\hat{v}	vertical velocity component, (m/s).
v	dimensionless vertical velocity component.
\hat{x}, \hat{y}	horizontal and vertical coordinates, (m).
x, y	dimensionless horizontal and vertical coordinates.

Greek symbols

α_r	thermal diffusivity ratio, $\alpha_r = \alpha_s / \alpha_f$.
ε	porosity.
θ	dimensionless temperature, $\theta = (\hat{T} - T_o) / (T_h - T_o)$.
μ_f	fluid dynamic viscosity, (kg/m s).
ρ_f	fluid density, (kg/m^3).
φ	angular coordinate, ($^\circ$).

Subscripts

eff	effective.
f	fluid.
o	inlet of the channel.
out	outlet of the channel.
s	solid.
t	total.

References

- [1] H.M. Badr, I. Pop, Combined convection from an isothermal horizontal rod buried in a porous medium, *International Journal of Heat and Mass Transfer* 31 (12) (1988) 2527–2541.
- [2] P. Cheng, Mixed convection about a horizontal cylinder and a sphere in a fluid-saturated porous medium, *International Journal of Heat Mass Transfer* 25 (8) (1982) 1245–1247.
- [3] A.J. Chorin, Numerical solution of the navier-stokes equations, *Mathematics of Computation* 22 (104) (1968) 745–762.
- [4] S. Ergun, Fluid flow through packed columns, *Chemical Engineering Progress* 48 (2) (1952) 89–94.
- [5] D.B. Ingham, I. Pop, *Transport Phenomenon in Porous Media*, vol. 2, Pergamon, Oxford, 1979.
- [6] D.B. Ingham, I. Pop, Natural convection about a heated horizontal cylinder in a porous medium, *Journal of Fluid Mechanics* 184 (1987) 157–181.
- [7] G.E. Karniadakis, M. Israeli, S.A. Orszag, High-order splitting methods for the incompressible navier-stokes equations, *Journal of Computational Physics* 97 (2) (1991) 414–443.
- [8] M. Kaviany, *Principles of Heat Transfer in Porous Media*. Springer-Verlag, New York, 1995.
- [9] S. Kimura, Transient forced convection heat transfer from a circular cylinder in a saturated porous medium, *International Journal of Heat and Mass Transfer* 32 (1) (1989) 192–195.
- [10] M. Layeghi, A. Nouri-Borujerdi, Fluid flow and heat transfer around circular cylinders in the presence and no-presence of porous media, *Journal of Porous Media* 7 (3) (2004) 239–247.
- [11] M. Layeghi, A. Nouri-Borujerdi, Darcy model for the study of the fluid flow and heat transfer around a cylinder embedded in porous media, *International Journal of Computational Methods in Engineering Science and Mechanics* 7 (5) (2006) 323–329.
- [12] J.H. Merkin, Free convection boundary layers on axi-symmetric and two-dimensional bodies of arbitrary shape in a saturated porous medium, *International Journal of Heat and Mass Transfer* 22 (10) (1979) 1461–1462.
- [13] V.D. Murty, M.P. Camden, C.L. Clay, D.B. Paul, A study of non-Darcian effects on forced convection heat transfer over a cylinder embedded in a porous medium, in: *Proceedings of the International Heat Transfer Conference* (1990), pp. 201–206 New York, USA.
- [14] K. Nasr, S. Ramadhani, R. Viskanta, Experimental investigation on forced convection heat transfer from a cylinder embedded in a packed bed, *Journal of Heat Transfer* 116 (1) (1994) 73–80.
- [15] D.A. Nield, A. Bejan, *Convection in Porous Media*, third ed. Springer Science + Business Media, New York, NY, USA, 2006.
- [16] I. Pop, P. Cheng, Flow past a circular cylinder embedded in a porous medium based on the brinkman model, *International Journal of Engineering Science* 30 (2) (1992) 257–262.
- [17] I. Pop, D.B. Ingham, *Convective Heat Transfer: Mathematical and Computational Modelling of Viscous Fluids and Porous Media*. Pergamon, Oxford, 2001.
- [18] I. Pop, B. Yan, Forced convection flow past a circular cylinder and a sphere in a darcian fluid at large peclet numbers, *International Communications in Heat and Mass Transfer* 25 (2) (1998) 261–267.
- [19] D.A.S. Rees, A.P. Bassom, I. Pop, Forced convection past a heated cylinder in a porous medium using a thermal non-equilibrium model: boundary layer analysis, *European Journal of Mechanics, B/Fluids* 22 (5) (2003) 473–486.
- [20] N.H. Saeid, Analysis of free convection about a horizontal cylinder in a porous media using a thermal non-equilibrium model, *International Communications in Heat and Mass Transfer* 33 (2) (2006) 158–165.
- [21] T. Sano, Unsteady heat transfer from a circular cylinder immersed in a darcy flow, *Journal of Engineering Mathematics* 14 (3) (1980) 177–190.
- [22] J. Thevenin, D. Sadaoui, About enhancement of heat transfer over a circular cylinder embedded in a porous medium, *International Communications in Heat and Mass Transfer* 22 (2) (1995) 295–304.
- [23] M.C. Thompson, K. Hourigan, A. Cheung, T. Leweke, Hydrodynamics of a particle impact on a wall, *Applied Mathematical Modelling* 30 (11) (2006) 1356–1369.
- [24] K. Vafai, *Handbook of Porous Media*. Marcel Dekker, New York, 2000.
- [25] K. Vafai, M. Sozen, Analysis of energy and momentum transport for fluid flow through a porous bed, *Transactions of the ASME Journal of Heat Transfer* 112 (3) (1990) 390–399.
- [26] N. Wakao, S. Kagueli, *Heat and Mass Transfer in Packed Beds*. Gordon and Breach, New York, 1982.
- [27] K.C. Wong, N.H. Saeid, Numerical study of mixed convection on jet impingement cooling in a horizontal porous layer under local thermal non-equilibrium conditions, *International Journal of Thermal Sciences* 48 (5) (2009) 860–870.
- [28] W.S. Wong, D.A.S. Rees, I. Pop, Forced convection past a heated cylinder in a porous medium using a thermal non-equilibrium model: finite peclet number effects, *International Journal of Thermal Sciences* 43 (3) (2004) 213–220.
- [29] P. Zehner, E.U. Schlunder, Thermal conductivity of granular materials at moderate temperatures, *Chemie-Ingenieur-Technik* 42 (14) (1970) 933–941.
- [30] M.J. Zhou, R.C. Lai, Aiding and opposing mixed convection from a cylinder in a saturated porous medium, *Journal of Porous Media* 5 (2) (2002) 103–111.